Advances in Water Resources xxx (2010) xxx–xxx

Contents lists available at ScienceDirect

Advances in Water Resources

journal homepage: www.elsevier.com/locate/advwatres

High-resolution numerical simulation of turbulence in natural waterways

Seokkoo Kang, Anne Lightbody [1], Craig Hill, Fotis Sotiropoulos *

St. Anthony Falls Laboratory, Department of Civil Engineering, University of Minnesota, 2 Third Avenue SE, Minneapolis, MN 55414, USA

ARTICLE INFO

Article history:
Received 3 June 2010
Received in revised form 24 September 2010
Accepted 30 September 2010
Available online xxxx

Keywords:
Navier–Stokes equation
Large-eddy simulation
Reynolds-averaged Navier–Stokes modeling
Immersed boundary method
Stream flow

ABSTRACT

We develop an efficient and versatile numerical model for carrying out high-resolution simulations of turbulent flows in natural meandering streams with arbitrarily complex bathymetry. The numerical model solves the 3D, unsteady, incompressible Navier–Stokes and continuity equations in generalized curvilinear coordinates. The method can handle the arbitrary geometrical complexity of natural streams using the sharp-interface curvilinear immersed boundary (CURVIB) method of Ge and Sotiropoulos (2007) [1]. The governing equations are discretized with three-point, central, second-order accurate finite-difference formulas and integrated in time using an efficient, second-order accurate fractional step method. To enable efficient simulations on grids with tens of millions of grid nodes in long and shallow domains typical of natural streams, the algebraic multigrid (AMG) method is used to solve the Poisson equation for the pressure coupled with a matrix-free Krylov solver for the momentum equations. Depending on the desired level of resolution and available computational resources, the numerical model can either simulate, via direct numerical simulation (DNS), large-eddy simulation (LES), or unsteady Reynolds-averaged Navier–Stokes (URANS) modeling. The potential of the model as a powerful tool for simulating energetic coherent structures in turbulent flows in natural river reaches is demonstrated by applying it to carry out LES and URANS in a 50-m long natural meandering stream at resolution sufficiently fine to capture vortex shedding from centimeter-scale roughness elements on the bed. The accuracy of the simulations is demonstrated by comparisons with experimental data and the relative performance of the LES and URANS models is also discussed.

1. Introduction

Natural streams and rivers are characterized by arbitrary geometrical complexity that spans a wide range of scales: from the scale of a stream or river meander, to the scale of transverse bathymetric variabilities, down to the scale of boulders, small rocks, and sand grains typically found in river beds. The presence of natural and/or man-made structures, such as riffles and pools, tree trunks, root wads, bridge foundations and stream restoration structures, and dynamically evolving boundaries (water surface and erodible bed) further add to the difficulty of the problem. These difficulties are daunting and render attempts to simulate turbulence in natural aquatic environments a rather challenging undertaking for even the most advanced numerical methods available today. Modeling difficulties are especially exacerbated when one is interested in resolving directly, rather than modeling with statistical approaches, the dynamics of energetic coherent vortical structures that dominate flows in natural waterways. Coherent vortical structures in such flows are induced by the aforementioned geometrical complexities and range from large-scale, slowly evolving eddies in regions of recirculation and flow stagnation to energetic shear layers, tornado and whirlpool type vortices, horseshoe vortices, and curvature-induced streamwise vortices. It has already been shown [2,3] that slowly evolving, large-scale vortical structures can be the primary mechanism for producing turbulence in flows past wall-mounted hydraulic structures. As such, being able to accurately simulate unsteady coherent structures in natural aquatic environments is a critical prerequisite not only for understanding scalar and particulate transport processes but also for facilitating a number of important engineering objectives. Examples include, among others, improved design of bridge foundations that are not susceptible to scour, stabilization of stream banks, quantification of nutrient residence times to evaluate denitrification potential, and the enhancement of aquatic habitat quality in stream restoration projects.

Due to the enormous geometrical complexity of natural waterways and the wide variability of spatial and temporal scales of the various coherent structures, accurate numerical simulations require fine computational meshes, small time steps and numerical algorithms that are versatile and efficient enough to handle all underlying complexities. A related major numerical difficulty stems from the fact that typical streams or rivers are very long, wide and shallow giving rise to computational domains with large

* Corresponding author.
E-mail address: fotis@umn.edu (F. Sotiropoulos).
[1] Present address: Department of Earth Sciences, University of New Hampshire, 56 College Road, Durham, NH 03824, USA.

0309-1708/$ - see front matter © 2010 Elsevier Ltd. All rights reserved.
doi:10.1016/j.advwatres.2010.09.018

aspect ratios. Unsteady flow simulations on fine computational grids in such large-aspect ratio domains can be plagued by numerical stiffness greatly degrading the efficiency of iterative solvers and rendering numerical simulations within reasonable computational times unlikely if not impossible even on powerful, massively parallel computational platforms. In this paper we report progress toward the development and demonstrate the potential and predictive capabilities of a numerical method that can tackle several of these challenges.

Numerical simulation of turbulent flows in natural rivers and streams has been the subject of intense research for well over 15 years. One of the first 3D models of flow in a natural reach was reported by Sinha et al. [4] who employed a multi-block approach with generalized curvilinear coordinates to simulate the flow in a 2.5 mile reach of the Columbia River downstream of the Wanapum Dam. They carried out steady Reynolds-averaged simulation (RANS) with the standard k–ε model with wall-functions and reported good agreement between the simulations and the results of a laboratory-scale model study. Wilson et al. [5] also employed RANS with the k–ε model to simulate the flow through a pseudo-natural meandering reach that was created in a laboratory environment and also reported good agreement between measured and computed mean velocity fields. Rodriguez et al. [6] reported RANS simulations of the flow in the 60-m reach of the Embarras River using Flow-3D™ software with the k–ε RNG model for turbulence closure. The numerical model was able to capture the secondary flow patterns developing in this highly sinuous reach. Lai et al. [7] solved a laboratory scale meandering open channel flow using the k–ε model and obtained mean streamwise and transverse velocities that agree well with the measured data. Zeng et al. [8] solved the flowfield and the transport of sediment in a sharp open channel bend using the Spalart–Allmaras model [9] and the SST model [10] and compared the computed velocities and bed elevation with measurements.

Steady RANS models, such as those discussed above, are efficient engineering simulation tools and have been shown to capture with reasonable accuracy the mean flow characteristics in natural rivers. However, such models are inherently incapable of resolving the dynamics of large-scale coherent structures and their impact on turbulence production and scalar and particulate transport. Unsteady RANS (URANS) models, which solve the RANS equations in a time accurate manner, can in principle capture large-scale, organized vortex shedding and such models have also been applied to simulate turbulence in natural waterways. Ge and Sotiropoulos [11], for instance, simulated the flow through a reach of the Chatachochee River near Cornelia, Georgia, with an embedded bridge foundation using an overset grid approach with the standard k–ε model in URANS mode. The model could capture large-scale vortex shedding from the bridge piers and the simulated mean velocity field was in good agreement with laboratory scale measurements [12]. In spite of encouraging results, however, the model yielded an essentially steady horseshoe vortex system in the vicinity of the bridge foundation, which is in contrast with experimental observations of Devenport and Simpson [2] and a direct consequence of the inherent excessive diffusivity of URANS type models.

Large-eddy simulation (LES) models and hybrid URANS/LES models can simulate the dynamics of coherent vortical structures and have been applied extensively to a wide range of engineering and hydraulic engineering flows. Hodges and Street [13] carried out LES for turbulent open channel flow with presence of free surface and Zedler and Street [14] carried out LES for flow over periodic ripples to study flow dynamics of the sediment transport. McCoy et al. [15] carried out LES for flow around multiple groynes in a straight, rectangular open channel. They obtained good agreement between computed and measured mean velocities and velocity variances. Recently Stoesser et al. [16] carried out both steady RANS simulation and LES to simulate turbulent flow in a meandering open channel consisting of two 180° bends and compared the computed mean velocity profile with laboratory measurements. The computed results correctly reproduced the presence of the secondary cells in the bend. Paik and Sotiropoulos [3] and Paik et al. [17] have successfully applied Detached Eddy Simulation (DES) [18], a hybrid URANS/LES model, to simulate the rich dynamics of coherent vortical structures past abutment and bridge-pier like structures mounted in straight rectangular open channels and reported good agreement between the simulations and experiments.

LES and hybrid URANS/LES models have been successful in resolving dynamically rich coherent vortices in open channels with complex hydraulic structures. However, such models typically require much finer computational grids than RANS and URANS models and thus drastically increase the computational cost. It is presumably due to this limitation that most previous attempts to simulate open channel flows with coherent-structure resolving turbulence models have been restricted to channels of simple topography or focused on the flow in the immediate vicinity of the in-stream structures. To the best of our knowledge, coherent-structure resolving simulations of flows in geometries exhibiting the complexities that characterize natural waterways, as discussed in the beginning of this section, have yet to be reported in the literature.

In this paper we report the development of a novel computational model that can carry out high-resolution simulations in open channel with arbitrarily complex bathymetry and multiple embedded in-stream structures. To tackle problems associated with the inherent geometric complexity of the problem, we extend the curvilinear immersed boundary (CURVIB) method [1] to carry out efficient URANS and LES simulations in meandering open channels. The efficiency of the original fractional-step solver [1] is improved by over one order of magnitude to enable practical simulations in large-aspect ratio computational domains discretized with fine computational grids. This is accomplished by employing the algebraic multigrid (AMG) method as a preconditioner for Krylov subspace method to solve the Poisson equation for the pressure field. Wall models are also incorporated into the method to facilitate both LES and URANS simulations in the context of the CURVIB method. The new method is validated by applying to simulate model flows in relatively simple geometries. The potential of the method as a powerful hydraulic engineering simulation tool is demonstrated by applying it to carry out both URANS and LES for turbulent flow in the natural-like meandering stream that is currently installed in the St. Anthony falls Laboratory Outdoor StreamLab (OSL). The stream bathymetry exhibits many of the complexities characterizing natural waterways and provides an excellent test-bed for demonstrating the capabilities of the model. It is important to emphasize that free-surface and streambed erosion effects are not considered in this work. We focus exclusively on flows over arbitrarily complex albeit rigid bed at relatively low Froude numbers for which the rigid lid assumption can be invoked to simulate the free-surface.

The paper is organized as follows. First we present the governing equations for the resolved flow and turbulence closure models. Subsequently we describe the numerical method we employ to solve these equations. This is followed by presentation of the results of validation studies and the application of the model to the OSL stream. Finally, we summarize our findings and discuss future work.

2. Governing equations and boundary conditions

2.1. Resolved flow equations

The equations governing the instantaneous, resolved flowfield for three-dimensional, incompressible, turbulent flow are the time

Please cite this article in press as: Kang S et al. High-resolution numerical simulation of turbulence in natural waterways. Adv Water Resour (2010), doi:10.1016/j.advwatres.2010.09.018

(Reynolds) or spatially-averaged (for URANS and LES, respectively) continuity and Navier–Stokes equations. In the curvilinear immersed boundary (CURVIB) method of Ge and Sotiropoulos [1] employed in this work, the governing equations are first written in Cartesian coordinates $\{x_i\}$ and then transformed fully (both the velocity vector and spatial coordinates are expressed in curvilinear coordinates) in non-orthogonal, generalized, curvilinear coordinates $\{\xi_i\}$. The transformed equations read in compact tensor notation (repeated indices imply summation) as follows ($i,j = 1,2,3$):

$$J\frac{\partial U_j}{\partial \xi_j} = 0, \tag{1}$$

$$\frac{1}{J}\frac{\partial U_i}{\partial t} = \frac{\xi_l^i}{J}\left(-\frac{\partial}{\partial \xi_j}(U_j u_l) + \frac{1}{\rho}\frac{\partial}{\partial \xi_j}\left(\mu \frac{g^{jk}}{J}\frac{\partial u_l}{\partial \xi_k}\right) - \frac{1}{\rho}\frac{\partial}{\partial \xi_j}\left(\frac{\xi_l^j p}{J}\right) - \frac{1}{\rho}\frac{\partial \tau_{lj}}{\partial \xi_j}\right), \tag{2}$$

where J is the Jacobian of the geometric transformation given by $J = |\partial(\xi_1,\xi_2,\xi_3)/\partial(x_1,x_2,x_3)|$, $\xi_l^i = \partial \xi_i/\partial x_l$ are the transformation metrics, u_i is the ith Cartesian velocity component, $U_i = \left(\xi_m^i/J\right)u_m$ is the contravariant volume flux, $g^{jk} = \xi_l^j \xi_l^k$ are the components of the contravariant metric tensor, p is the pressure, ρ is the density, μ is the dynamic viscosity, and τ_{ij} is the sub-grid stress tensor for LES models or the Reynolds stress tensor for RANS models.

2.2. Turbulence models

We employ both LES and URANS turbulence models in this work implemented in the context of the CURVIB method so that they can be applied to arbitrarily complex geometric configuration. The governing equations for these models are described in this section and the implementation of those models in the context of the CURVIB method will be discussed in detail in Section 4.

2.2.1. LES model

The filtered Navier–Stokes equations (Eqs. (1) and (2)) are obtained by decomposing the velocity into resolved and unresolved components and integrating the Navier–Stokes equations over the spatial filter [19]. As a result, sub-grid stress terms appear in the momentum equations (Eq. (2)), which are modeled using the Smagorinsky sub-grid scale (SGS) model [20]

$$\tau_{ij} - \frac{1}{3}\tau_{kk}\delta_{ij} = -2\mu_t \overline{S_{ij}}, \tag{3}$$

where the overbar denotes the grid filtering operation, and $\overline{S_{ij}}$ is the filtered strain-rate tensor. The eddy viscosity is given by

$$\mu_t = C_s \Delta^2 |\overline{S}|, \tag{4}$$

where C_s is the Smagorinsky constant, Δ is the filter size, and $|\overline{S}| = \sqrt{2\overline{S_{ij}}\,\overline{S_{ij}}}$. The box filter [19] is employed in the present model, which is given as follows:

$$\Delta = J^{-1/3}. \tag{5}$$

In the above equation J^{-1} represents the cell volume, and the filter size is taken as the cubic root of the cell volume.

We employ the dynamic Smagorinsky model [21] as a sub-grid model in which the model constant C_s evolves in spaces and time as function of the flow. The optimal value of C_s is selected to minimize the mean square error between the resolved stress at the grid filter and the test filter [21] as follows:

$$C_s = \frac{\langle L_{ij} M_{ij}\rangle}{\langle M_{kl} M_{kl}\rangle}, \tag{6}$$

where

$$L_{ij} = \widehat{\overline{u_i}\,\overline{u_j}} - \widehat{\overline{u}_i}\,\widehat{\overline{u}_j}, \tag{7}$$

$$M_{ij} = 2\Delta^2 \widehat{\overline{S_{ij}}|\overline{S}|} - 2\widehat{\Delta}^2 \widehat{\overline{S_{ij}}}\,\widehat{|\overline{S}|}. \tag{8}$$

In the above equations, $\widehat{\Delta}$ is the size of the test filter which is twice larger than the grid filter for uniform grids and the hat denotes the test filtering, which in three-dimensions involves the 27 grid nodes surrounding a given grid node. $\langle\rangle$ means averaging in the homogeneous directions. The homogeneous direction implies the direction where the periodic boundary condition is employed. For problems with no homogeneous direction present (fully three-dimensional cases) this averaging can be replaced by local averaging around a grid node.

It was pointed out in [22] that Eq. (6) is not invariant with respect to a rotation of the frame of the reference in generalized curvilinear coordinates. To remedy this, the following invariant formulation [22] is employed in this work:

$$C_s = \frac{\langle L_{il} M_{im} G_{lm}\rangle}{\langle M_{kp} M_{kq} G_{pq}\rangle}, \tag{9}$$

where G_{lm} is the covariant metric tensor.

In the present numerical implementation of the above SGS model, the Smagorinsky constant and the eddy viscosity are computed at the center of the cell using Eqs. (9) and (4), respectively, at the beginning of each time step. Subsequently the eddy viscosity is interpolated from the cell center to the cell face and it is used to calculate the SGS terms in Eq. (3).

2.2.2. URANS models

In URANS models the τ_{ij} tensor in Eq. (2) is the Reynolds stress tensor, which is modeled using the Boussinesq hypothesis as follows:

$$\tau_{ij} = -2\mu_t \widetilde{S_{ij}} + \frac{2}{3}\rho k \delta_{ij}, \tag{10}$$

where $\widetilde{S_{ij}}$ is the Reynolds averaged strain-rate tensor, μ_t is the eddy viscosity, k is the turbulence kinetic energy, and δ_{ij} is the unit tensor. To close the URANS equations, we employ both the k–ω model [23] and the SST model [10].

The governing equations for the k–ω model [23] are formulated in generalized curvilinear coordinates as follows:

$$\frac{1}{J}\frac{\partial(\rho k)}{\partial t} + \frac{\partial}{\partial \xi_j}(\rho k U_j) = \tau_{ij}\frac{\xi_j^k}{J}\frac{\partial u_i}{\partial \xi_k} - \frac{1}{J}\beta^* \rho k \omega + \frac{\partial}{\partial \xi_j}\left((\mu + \sigma^* \mu_t)\frac{g^{jk}}{J}\frac{\partial k}{\partial \xi_k}\right), \tag{11}$$

$$\frac{1}{J}\frac{\partial(\rho \omega)}{\partial t} + \frac{\partial}{\partial \xi_j}(\rho \omega U_j) = \alpha\frac{\rho\omega}{k}\tau_{ij}\frac{\xi_j^k}{J}\frac{\partial u_i}{\partial \xi_k} - \frac{1}{J}\beta \rho \omega^2 + \frac{\partial}{\partial \xi_j}\left((\mu + \sigma^* \mu_t)\frac{g^{jk}}{J}\frac{\partial \omega}{\partial \xi_k}\right), \tag{12}$$

$$\mu_t = \rho k/\omega, \tag{13}$$

where the closure coefficients are given as $\alpha = 5/9$, $\beta = 3/40$, $\beta^* = 9/100$, $\sigma = 1/2$, and $\sigma^* = 1/2$.

The governing equations for the SST model [10] in generalized curvilinear coordinates read as follows:

$$\frac{1}{J}\frac{\partial(\rho k)}{\partial t} + \frac{\partial}{\partial \xi_j}(\rho k U_j) = \frac{1}{J}\widetilde{P} - \frac{1}{J}\beta^* \rho k \omega + \frac{\partial}{\partial \xi_j}\left((\mu + \sigma_k \mu_t)\frac{g^{jk}}{J}\frac{\partial k}{\partial \xi_k}\right), \tag{14}$$

Please cite this article in press as: Kang S et al. High-resolution numerical simulation of turbulence in natural waterways. Adv Water Resour (2010), doi:10.1016/j.advwatres.2010.09.018

$$\frac{1}{J}\frac{\partial(\rho\omega)}{\partial t}+\frac{\partial}{\partial\xi_j}(\rho\omega U_j)=\frac{1}{J}\alpha\rho\widetilde{S}^2-\frac{1}{J}\beta\rho\omega^2+\frac{\partial}{\partial\xi_j}\left((\mu+\sigma_\omega\mu_t)\frac{g^{jk}}{J}\frac{\partial\omega}{\partial\xi_k}\right)+\frac{1}{J}2(1-F_1)\rho\sigma_{\omega2}\frac{1}{\omega}\left(\frac{\partial\xi_l}{\partial x_j}\frac{\partial k}{\partial\xi_l}\right)\left(\frac{\partial\xi_l}{\partial x_j}\frac{\partial\omega}{\partial\xi_l}\right), \quad (15)$$

$$\mu_t=\frac{a_1\rho k}{max(a_1\omega,SF_2)}, \quad (16)$$

where $\widetilde{S}=\sqrt{2\widetilde{S_{ij}}\widetilde{S_{ij}}}$ is the invariant measure of the strain rate and $\widetilde{P}$ is a limited production term given by the following equation:

$$\widetilde{P}=min\left(\mu_t\frac{\partial u_i}{\partial x_j}\left(\frac{\partial u_i}{\partial x_j}+\frac{\partial u_j}{\partial x_i}\right),10\beta^*\rho k\omega\right). \quad (17)$$

F_1 and F_2 are blending functions defined by

$$F_1=tanh\left\{\left\{min\left[max\left(\frac{\sqrt{k}}{\beta^*\omega d},\frac{500\mu}{\rho d^2\omega}\right),\frac{4\rho\sigma_{\omega2}k}{CD_{k\omega}d^2}\right]\right\}^4\right\}, \quad (18)$$

$$F_2=tanh\left[\left[max\left(\frac{2\sqrt{k}}{\beta^*\omega d},\frac{500\mu}{\rho d^2\omega}\right)\right]^2\right] \quad (19)$$

with

$$CD_{k\omega}=max\left(2\rho\sigma_{\omega2}\frac{1}{\omega}\frac{\partial k}{\partial x_j}\frac{\partial\omega}{\partial x_j},10^{-10}\right), \quad (20)$$

and d is the distance to the nearest wall.

The closure coefficients of the SST model are obtained by blending those of the k–ω model, denoted as ϕ_1, and the standard k–ϵ model, denoted as ϕ_2, via the relation $\phi=\phi_1F_1+\phi_2(1-F_1)$. The coefficients are given by $a_1=0.31$, $\beta^*=9/100$, $\alpha_1=5/9$, $\beta_1=3/40$, $\sigma_{k1}=0.85$, $\sigma_{\omega1}=0.5$, $\alpha_2=0.44$, $\beta_2=0.0828$, $\sigma_{k2}=1$, $\sigma_{\omega2}=0.856$.

Third-order WENO [24] and second-order central differencing schemes are used for the spatial discretization of advection and diffusion terms in k and ω equations, respectively, and the second-order backward differencing scheme is used for the time integration. The k and ω equations of k–ω and SST models are solved at every time step after the velocity fields are obtained by the subsequently described fractional step method. The values of eddy viscosity are calculated at the center of the cell using Eq. (16), and they are interpolated to the face of the cell. The fully implicit Jacobian-free Newton's method is employed for solving Eqs. (11) and (12) or Eqs. (14) and (15) in order to enhance numerical stability. This implicit method alleviates the numerical instability caused by the presence of stiff source terms in the k and ω equations. The fully implicit Jacobian-free Newton's method is also used for solving the momentum equations and will be described in Section 3.2.

2.3. Boundary conditions near solid walls

In high Reynolds number flow simulations, applying the no-slip boundary condition at the wall is often impractical as it results in excessively fine meshes and long computational times. To address this difficulty in this work we employ the wall model proposed in [25,26]. The model solves the boundary layer equation in the following form:

$$\frac{1}{\rho}\frac{\partial}{\partial l}\left((\mu+\mu_t)\frac{\partial u_s}{\partial l}\right)=\frac{1}{\rho}\frac{\partial p}{\partial s}+\frac{\partial u_s}{\partial t}+\frac{(\partial u_l u_s)}{\partial s}, \quad (21)$$

where l and s indicate the directions normal and tangential to the wall, respectively. By neglecting the right hand side of the Eq. (21), one obtains the equilibrium stress balance model [26]

$$\frac{1}{\rho}\frac{\partial}{\partial l}\left((\mu+\mu_t)\frac{\partial u_{si}}{\partial l}\right)=0. \quad (22)$$

The eddy viscosity is given by the mixing length model with the near-wall damping as

$$\mu_t=\mu\kappa l^+(1-e^{-l^+/19})^2, \quad (23)$$

where $l^+=\rho u_\tau l/\mu$ and u_τ is the wall shear velocity. Eq. (22) is integrated from the wall to the second off-wall node to obtain the tangential velocity at the first off-wall node. The implementation of this model in the context of the CURVIB method is discussed in Section 4.1.

3. Numerical integration of the Navier–Stokes equations

3.1. The fractional step method

To solve the resolved flow equations, Eqs. (1) and (2), we employ the implicit fractional step method proposed by Ge and Sotiropoulos [1]. During the first step, the momentum equations (Eq. (2)) are discretized in a fully implicit manner using second-order backward differencing in time:

$$\frac{1}{J}\frac{3\mathbf{U}^*-4\mathbf{U}^n+\mathbf{U}^{n-1}}{2\Delta t}=RHS(\mathbf{U}^*,\mathbf{u}^*), \quad (24)$$

where n denotes the time level and RHS is the right hand side of Eq. (2). Both advection and diffusion terms in the right hand side of Eq. (24) are discretized using, three-point central, second-order accurate finite-differencing.

The intermediate velocity field U^* obtained by solving Eq. (24) is not divergence-free and needs to be corrected to satisfy the continuity equation. This is accomplished by formulating and solving the following Poisson equation for the pressure increment (or pressure correction) $\phi=p^{n+1}-p^n$:

$$-J\frac{\partial}{\partial\xi_i}\left(\frac{1}{\rho}\frac{\xi_l^i}{J}\frac{\partial}{\partial\xi_j}\left(\frac{\xi_l^j\phi}{J}\right)\right)=\frac{3}{2\Delta t}J\frac{\partial U_j^*}{\partial\xi_j}. \quad (25)$$

Following the solution of the above equation (see below), the pressure and contravariant volume fluxes are obtained as follows:

$$p^{n+1}=p^n+\phi, \quad (26)$$

$$U_i^{n+1}=U_i^*-J\frac{2\Delta t}{3}\frac{1}{\rho}\frac{\xi_l^i}{J}\frac{\partial}{\partial\xi_j}\left(\frac{\xi_l^j\phi}{J}\right). \quad (27)$$

The above fractional step algorithm is implemented discretely in a hybrid staggered/non-staggered grid, which was originally proposed by Gilmanov and Sotiropoulos [27] for Cartesian grids and subsequently extended to curvilinear coordinates by Ge and Sotiropoulos [1]. The formulation is such that it satisfies the discrete divergence of the velocity field to machine zero in generalized curvilinear grids. For details the reader is referred to Ge and Sotiropoulos [1].

3.2. Solution of the discrete momentum equation

The discretized momentum equation given by Eq. (24) is a nonlinear ordinary differential equation for $\mathbf{U}^*$ that can be written as follows:

$$F(\mathbf{U})=0, \quad (28)$$

where F is a general functional involving both the time derivative and the right hand side of Eq. (24) and the superscript * from Eq. (24) is omitted for brevity. To linearize the functional $F(\mathbf{U})$ we expand it in a Taylor series about $\mathbf{U}=\mathbf{U}^k$ (where $\mathbf{U}^k$ is the

Please cite this article in press as: Kang S et al. High-resolution numerical simulation of turbulence in natural waterways. Adv Water Resour (2010), doi:10.1016/j.advwatres.2010.09.018

approximation to the final solution $\mathbf{U}^*$ during the k iteration). Neglecting the higher-order terms yields the Newton's method

$$A(\mathbf{U}^k)\delta\mathbf{U}^k = -F(\mathbf{U}^k), \tag{29}$$

$$\mathbf{U}^{k+1} = \mathbf{U}^k + \delta\mathbf{U}^k, \tag{30}$$

where A is the Jacobian matrix of F given by $A(\mathbf{U}^k) = F'(\mathbf{U}^k)$. During each iteration k (denoted as outer iteration) the now linear system given by Eq. (29) is solved by using the GMRES method [28]. The procedure that solves the linear system is called the inner iteration. When the GMRES method is used as a linear solver for the inner iteration, the Jacobian matrix does not need to be stored since it only requires matrix–vector products which can be approximated by a simple finite difference method, as follows:

$$A\mathbf{x} = \frac{F(\mathbf{U} + \epsilon\mathbf{x}) - F(\mathbf{U})}{\epsilon}, \tag{31}$$

where ϵ is a small scalar perturbation. The method shown in [29] is employed to compute ϵ. Since Jacobian-free methods do not require assembling and storing the Jacobian matrix, it is appropriate for problems with large number of unknowns. At each time step, outer and inner iterations are repeated until the residuals satisfy the following convergence criterion:

$$\|\mathbf{r}^k\|_2 = \|A(\mathbf{U}^k)\delta\mathbf{U}^k + F(\mathbf{U}^k)\|_2 \leqslant \eta_k\|F(\mathbf{U}^k)\|_2, \tag{32}$$

where $\eta_k \in (0,1)$ is a forcing term that controls the convergence of the solution. Instead of using a constant value of the forcing term, we employed the techniques proposed in [30] for computing η_k at each iteration, which significantly improves the convergence of the iterative scheme.

It is important to emphasize, however, that the above Newton's method converges only when the initial guess is sufficiently close to the exact solution. To make Newton's method globally convergent, one often needs a globalization method that brings the initial iterate into the radius of convergence of Newton's method [31]. The line search method [32] is employed in this work for the globalization of the Newton–Krylov method.

The GMRES method used in this study does not employ a preconditioner. We found that the solution of the momentum equation by using the Jacobian-free method without a preconditioner usually converges faster than the method with a preconditioner because the computational cost for forming the preconditioner at all inner iterations is significant.

The procedure described above solves the momentum equation in a fully implicit manner which greatly improves the stability of the numerical scheme and removes the CFL (Courant–Friedrichs–Lewy) time step restriction. It is important to point out that for LES the size of the time step is usually restricted by the smallest of the time-scale of the smallest resolvable eddies on a given grid and the viscous (diffusive) time scale but not by the CFL condition. Therefore, implicit treatment of the viscous terms along with explicit treatment of the convective terms is typically adequate for stable and efficient LES. In this study, however, we choose a fully implicit formulation to enhance the generality of the method and in particular its applicability to fine-mesh URANS simulations for which the CFL condition could be quite restrictive.

3.3. Algebraic multigrid (AMG) method for the Poisson equation

As already discussed in Section 1, a major challenge for carrying out reach-scale, high-resolution simulations of turbulence in natural waterways stems from the large aspect-ratio of the resulting computational domains due to the large disparity in flow depth the streamwise and lateral dimensions of the reach. Large domain and grid cell aspect-ratios induce numerical stiffness and could dramatically deteriorate the convergence rate of powerful iterative algorithms such as the previously described GMRES method [28]. This is an especially critical issue for the solution of the Poisson equation that needs to be satisfied to machine zero during every time step in order to satisfy the incompressibility condition for the velocity field. To improve the convergence of the Poisson equation in large aspect-ratio grids and domains, we employ the algebraic multigrid (AMG) as the preconditioner for the GMRES method [28]. The multigrid (MG) method has been one of the most successful methods for accelerating the convergence of elliptic equation solvers, and particularly geometric multigrid (GMG) methods have been popular for the simulation of incompressible flows with structured grids [1,33]. In the GMG, the convergence is accelerated by correcting the solution of the fine grid by solving an error residual equation on the coarser grid. Often more than two grid levels are employed, and the coarse grid usually is twice as coarse as the grid spacing of the next finer level grid. More details about the implementation of GMG can be found in [34]. The drawback of the GMG is that the convergence rate degenerates as the grid becomes more stretched and cell aspect ratio increases. The method with semi-coarsening has shown promise in simulations involving stretched, large aspect-ratio grids [35,36,1] but convergence could still be sluggish in generalized curvilinear grids and large aspect-ratio domains. In fact our initial attempts to employ GMG in this work were not successful as we found that the computational resources required to converge the Poisson equation were so large that high-resolution simulations of turbulence in real-life streams were impractical.

The AMG does not utilize the geometric information to build coarse grids, instead the adjacency graph of the matrix to be inverted is used. For example, we say that the point i strongly depends on j and vice versa if [37]

$$-a_{ij} \geqslant \alpha \max_{k\neq i}(-a_{ik}), \tag{33}$$

where a_{ij} is the component of a matrix at the ith row and the jth column and $\alpha \in (0,1)$ is a strength threshold. The above criterion was employed in the Ruge–Stüben coarsening algorithm [37] for building the coarse grid matrix. Details can be found in [37,38]. The underlying idea behind using the threshold α in Eq. (33) is very similar to that of the semi-coarsening method of the GMG, which generates coarse grids by neglecting the geometrically stretched directions, but is more general since it is not dependent on the geometric shape of the grid. For this reason, the AMG is more appropriate method for solving problems with complicated geometry and is employed in this work. In the present solver we implement AMG by employing the BoomerAMG package [38] with the parallel modified independent set (PMIS) coarsening scheme [39].

To demonstrate the drastic efficiency improvements that can be obtained with AMG, we employ the fractional step method described above to simulate impulsively started laminar flow through a very long square duct whose cross-section is intentionally discretized with highly stretched and distorted grids as shown in Fig. 1. This unusual grid structure is employed in order to set up a challenging numerical experiment combining a large-aspect ratio domain (streamwise length to width ratio equal to 10^3) with highly stretched and skewed grids.

The length of the computational domain in the x-, y- and z-directions is 1, 1 and 1000, respectively, and the number of grid points in each direction is 65. The flow is directed along the positive z-direction. While uniform grid spacing with a size of $\Delta z = 15.625$ is used in the z-direction, non-uniform, stretched grid is employed in x- and y-directions. The maximum and minimum grid spacing in x- and y-directions is 0.0761 and 0.001, respectively. The maximum $\Delta z/\Delta x$ ratio and the ratio of the maximum Δx to the minimum Δx are given by $max(\Delta z/\Delta x) = 15625$ and $max(\Delta x)/min(\Delta x) = 76.1$.

Please cite this article in press as: Kang S et al. High-resolution numerical simulation of turbulence in natural waterways. Adv Water Resour (2010), doi:10.1016/j.advwatres.2010.09.018

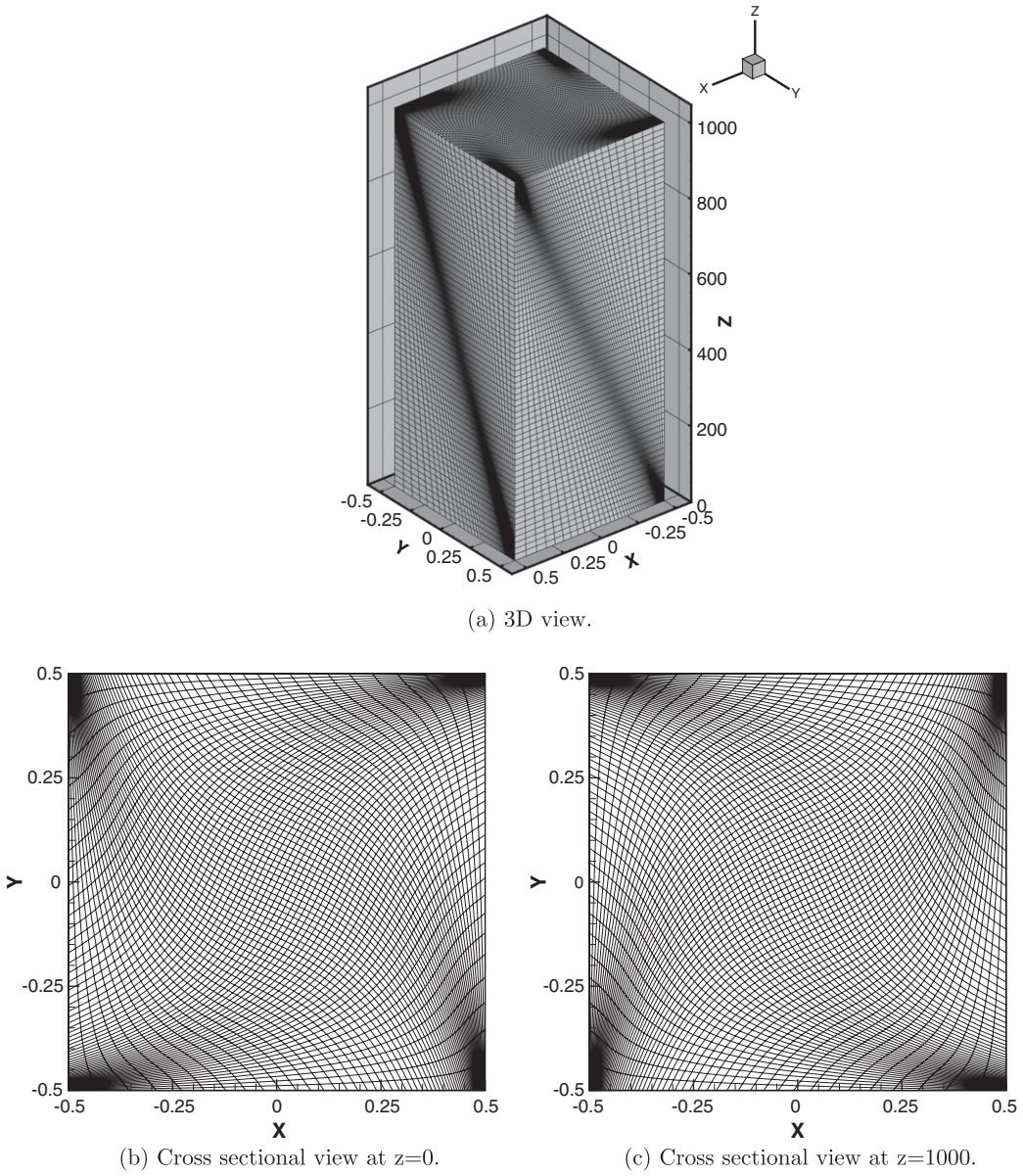

(a) 3D view.

(b) Cross sectional view at z=0.

(c) Cross sectional view at z=1000.

Fig. 1. Grid used for testing the efficiency of the AMG solver.

The Reynolds number based on the width of the duct and the mean velocity is 100 and the Poisson equation is solved with four different algorithms: AMG; GMG with 3-level semi-coarsening; GMG with 6-level semi-coarsening; and no multigrid. Four processors are used for the computation. The convergence history is shown in Fig. 2. It is evident that the no-multigrid option fails to converge while the GMG algorithm does improve the convergence rate somewhat especially when the number of grid coarsening levels is increased. Even for the 6-level GMG algorithm, however, the Poisson equation does not reach machine zero. Only with AMG the iterative algorithm converges monotonically to machine zero in just a fraction of a second of computational time. These results clearly show that large aspect ratios, grid stretching in multiple directions, and grid non-orthogonality cannot be easily treated by the standard semi-coarsening method of the GMG and establish the superior efficiency of the AMG over the GMG. The efficiency gains documented in Fig. 2 become even more significant in the context of applying AMG to solve the Poisson equation in a LES when several thousands of time steps need to be realized computationally to obtain statistically converged flowfields.

4. The CURVIB method for simulating turbulence in open channel flows

The CURVIB method [1] was originally proposed for cardiovascular flow applications in which a moving immersed boundary, e.g. a mechanical heart valve, is embedded in a background domain that can be efficiently discretized with a boundary-fitted curvilinear mesh (e.g. a curved blood vessel). Rather than using a boundary conforming mesh to describe the immersed moving boundary, the CURVIB methods treat the boundary as a sharp interface and boundary conditions are re-constructed at curvilinear grid nodes in the immediate vicinity of the boundary using interpolation along the local normal to the boundary direction [1,27]. So far the method has been applied to carry out direct numerical simulations of cardiovascular flows involving fluid structure interaction [40] and swimming of fish and planktonic organisms [41,42]. The CURVIB framework, however, is ideally suited for simulating flows in natural meandering streams with arbitrarily complex bed topography and in-stream structures. A schematic illustrating the application of the CURVIB method for a meandering stream is shown in

Please cite this article in press as: Kang S et al. High-resolution numerical simulation of turbulence in natural waterways. Adv Water Resour (2010), doi:10.1016/j.advwatres.2010.09.018

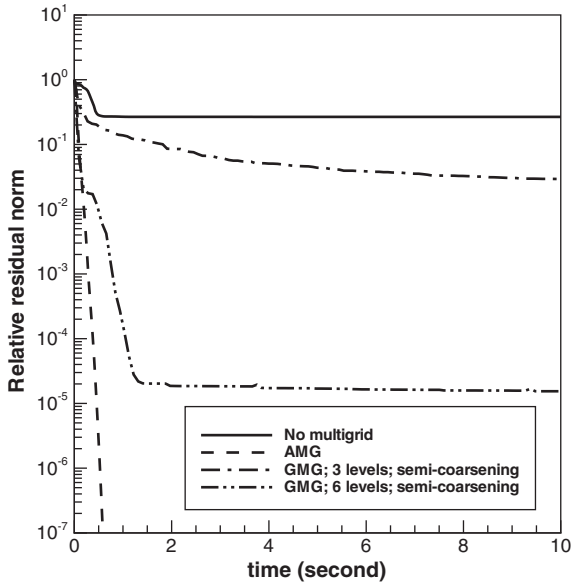

Fig. 2. Convergence of the Poisson equation.

Fig. 3. The immersed boundaries (bathymetry and in-stream structures) are discretized with a triangulated surface mesh and embedded in a curvilinear domain that follows the meandering outline of the stream but has a regular (prismatic) cross-section that contains fully the actual stream everywhere. In this section we describe the details of the method by emphasizing the new algorithmic developments implemented in this work to extend it to turbulent flow simulations.

The standard CURVIB method [1] employs wall normal interpolation for calculating the velocity components at near-wall grid nodes – referred to as immersed boundary (IB) grid nodes – under the hybrid staggered/non-staggered grid layout proposed by Gilmanov and Sotiropoulos [27]. Fig. 4 illustrates the wall normal interpolation for a velocity component or a turbulence quantity. At a given node (*B* in Fig. 4) immediately adjacent to the immersed boundary, a straight line is drawn normal to the nearest wall (*A* in Fig. 4) until it intersects with the grid line (or plane in 3D) which connects two (three in 3D) neighboring internal nodes. The point *C* in Fig. 4 is called the interception point. The values of flow variables at the point *C* are obtained by linear interpolation from computed values at internal grid nodes α and β. Gilmanov and Sotiropoulos [27] used the above approach to compute the velocity at the IB nodes in a manner such that the no-slip boundary condition is exactly satisfied at the wall. They used linear and quadratic interpolation which for turbulent flows would work well only if the grid spacing in the vicinity of the immersed boundary is sufficiently fine to resolve the laminar sublayer region and directly impose the no-slip condition on the solid immersed boundary. When the mesh is not sufficiently fine (as is often the case for high Reynolds number turbulent flows), however, the wall model described in Section 2.3 is used to reconstruct the boundary conditions. In what follows we describe the implementation of boundary conditions in the CURVIB method for both velocity components and turbulence quantities.

4.1. Velocity boundary conditions

As discussed above, the no-slip boundary condition is employed when the near wall grid spacing is fine enough to resolve the viscous sublayer. Assuming the velocity component at the solid wall (point *A*) is u_i^A, which is zero when the wall is not moving, and its distribution along the points *A*, *B* and *C* is linear, the Cartesian velocity components at the IB node is given as follows:

$$u_i^B = \left(\frac{\overline{AB}}{\overline{AC}}\right)(u_i^C - u_i^A) + u_i^A, \tag{34}$$

where $i = 1$, 2, and 3, and $\overline{AB}$ and $\overline{AC}$ denote the distance between the points *A* and *B* and the points *A* and *C*, respectively.

When the near wall grid spacing is not fine enough to resolve the viscous sublayer, the velocity boundary condition is obtained by the wall modeling approach. Integration of Eq. (22) from the surface of the wall at $l = 0$ to the second off-wall node at $l = \delta_c$ (*C* in Fig. 4) yields the following nonlinear equation:

$$\tau_w = \mu \left.\frac{\partial u_s}{\partial l}\right|_{l=0} = \frac{1}{\int_0^{\delta_c} \frac{1}{\mu+\mu_t} dl}(u_s(\delta_c) - u_s(0)), \tag{35}$$

$$\rho u_\tau^2 = \tau_w, \tag{36}$$

where δ_c is the distance from the wall to the node *C* and τ_w is the wall shear stress component in the tangential direction to the wall.

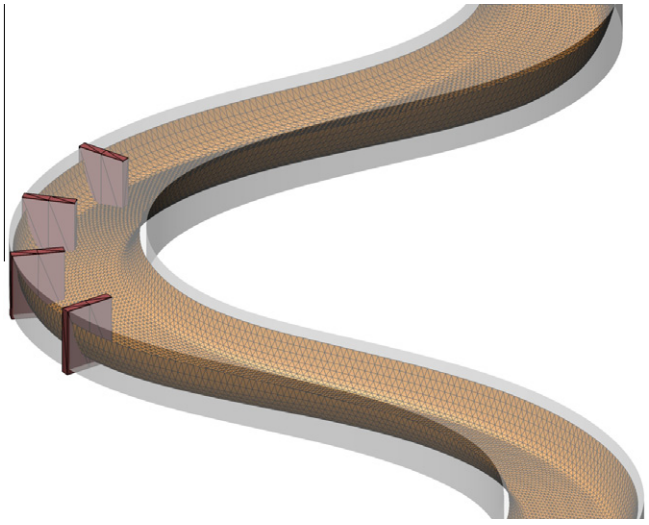

Fig. 3. Schematic description of applying the CURVIB method for the natural stream.

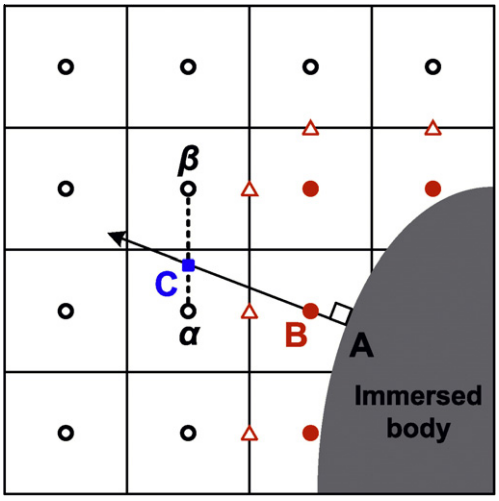

Fig. 4. Schematic description of the wall normal interpolation at the IB node (circles filled with red color: IB nodes, circles without fill: internal nodes, square filled with blue color: interception node, triangles: cell faces where the volume flux is stored).

Please cite this article in press as: Kang S et al. High-resolution numerical simulation of turbulence in natural waterways. Adv Water Resour (2010), doi:10.1016/j.advwatres.2010.09.018

The tangential direction s is determined from the velocity vector at the second off-wall node. The unit vector tangential to the wall is given by

$$s_i = \frac{u_i^C - \left(u_j^C l_j\right) l_i}{\left|u_i^C - \left(u_j^C l_j\right) l_i\right|}, \tag{37}$$

where n_i is the unit vector normal to the wall. The tangential velocity component at the wall is given by

$$u_s(0) = u_j^A s_j, \tag{38}$$

which is zero when the wall is stationary.

Eq. (35) is solved iteratively for u_τ using Newton's method. Usually 4 or 5 iterations are sufficient to get the converged solution. Once u_τ is computed, the tangential velocity component at the first off wall node (B in Fig. 4) is obtained by

$$u_s(\delta_b) = \frac{\int_0^{\delta_b} \frac{1}{\mu+\mu_t} dl}{\int_0^{\delta_c} \frac{1}{\mu+\mu_t} dl} (u_s(\delta_c) - u_s(0)) + u_s(0), \tag{39}$$

where δ_b is the distance from the wall to the node B. The normal velocity component at the IB nodes is obtained by the wall normal linear interpolation method. The above procedure is employed both for RANS and LES models. Although in this work the wall modeling method will be applied to solve problems involving only stationary immersed bodies, it is designed to be readily applicable to flow problems involving moving immersed bodies such as those encountered in fluid–structure interaction problems.

4.2. k and ω boundary conditions

The low Reynolds number wall boundary conditions for k and ω are [43]

$$k = 0, \tag{40}$$

$$\omega = \frac{6\mu}{\rho\beta d^2}, \tag{41}$$

where d is the wall distance at the first off-wall grid which is $\overline{AB}$ in Fig. 4. The above boundary conditions are adopted when the first off wall grid point is located inside the viscous sublayer. To impose the boundary condition given by Eq. (40) at the wall (A in Fig. 4), the linear interpolation along the line normal to the wall is employed. Assuming $k = 0$ at the node A one obtains the value of k at the IB node (B in Fig. 4)

$$k^B = \left(\frac{\overline{AB}}{\overline{AC}}\right) k^C. \tag{42}$$

The high Reynolds number wall boundary conditions for k and ω are [43]

$$k = \frac{u_\tau^2}{\sqrt{\beta^*}}, \tag{43}$$

$$\omega = \frac{u_\tau}{\sqrt{\beta^*}\kappa d}, \tag{44}$$

where $\kappa = 0.4$ is the von Kármán constant and u_τ is the wall shear velocity calculated by solving Eqs. (35) and (36). The above boundary conditions are adopted when the first off wall grid point is located inside the logarithmic layer. The boundary conditions given by Eqs. (41)–(44) are directly imposed at the IB node after wall shear velocity has been obtain from the previously described iterative procedure for obtaining the velocity boundary conditions.

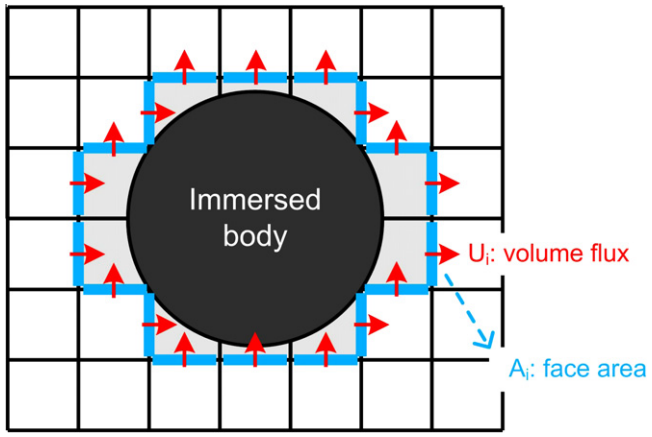

Fig. 5. Schematic description of the flux correction at the IB nodes.

4.3. Correction of velocity boundary conditions for global mass conservation

The previously described reconstruction techniques are used to specify velocity boundary conditions for the intermediate velocity field U^* in order to solve the momentum equation (Eq. (2)). The so resulting velocity field U^* does not satisfy the integral global mass conservation condition since this condition is not imposed either in the reconstruction of boundary conditions or in the solution of the momentum equation. As such, the pressure Poisson equation in Eq. (25) is ill posed, the so-called compatibility condition for Poisson equations is violated, and any attempt to solve it numerically will not converge. To remedy this situation, we propose a correction of the velocity boundary conditions at the IB nodes based on an area weighted volume flux approach. Fig. 5 illustrates in a schematic how this correction is implemented. The light gray areas denote the IB nodes, and the arrows denote the contravariant volume flux adjacent to both an IB node and a fluid node. To satisfy the global mass conservation the sum of all volume fluxes over a closed surface that surrounds a solid boundary, as shown in Fig. 5, must be zero. To satisfy this condition, the sum of the volume fluxes weighted by the ratio of the local face area (blue[2] areas in Fig. 5) to the total area is subtracted from the individual volume fluxes. Mathematically, this correction is formulated as follows:

$$\widetilde{U^*}_i = U_i^* - A_i \left(\frac{\sum_k U_k^*}{\sum_k A_k}\right), \tag{45}$$

where i denotes the cell face whose volume flux is being corrected, A_i is the area of the cell face adjacent to an IB node and a fluid node (blue areas in Fig. 5), U is the contravariant volume flux before correction, the index k spans all cell faces (all blue areas in Fig. 5) adjacent to both an IB node and a fluid node, and $\widetilde{U^*}$ is the corrected boundary flux used to calculate the right hand side of Eq. (25).

5. Results and discussion

In this section, we present results aimed at: (1) validating the numerical method; and (2) demonstrating its ability to carry out reach-scale, coherent-structure resolving simulations in waterways of arbitrarily complex bathymetry. To demonstrate the accuracy of the various facets of the method we first present simulations for three model problems solved using DNS, RANS, and LES, respectively. Subsequently we carry out URANS and LES for flow in a natural stream, compare the results with measurements and discuss the relative performance of the various models.

[2] For interpretation of color in Figs. 3–16, the reader is referred to the web version of this article.

Please cite this article in press as: Kang S et al. High-resolution numerical simulation of turbulence in natural waterways. Adv Water Resour (2010), doi:10.1016/j.advwatres.2010.09.018

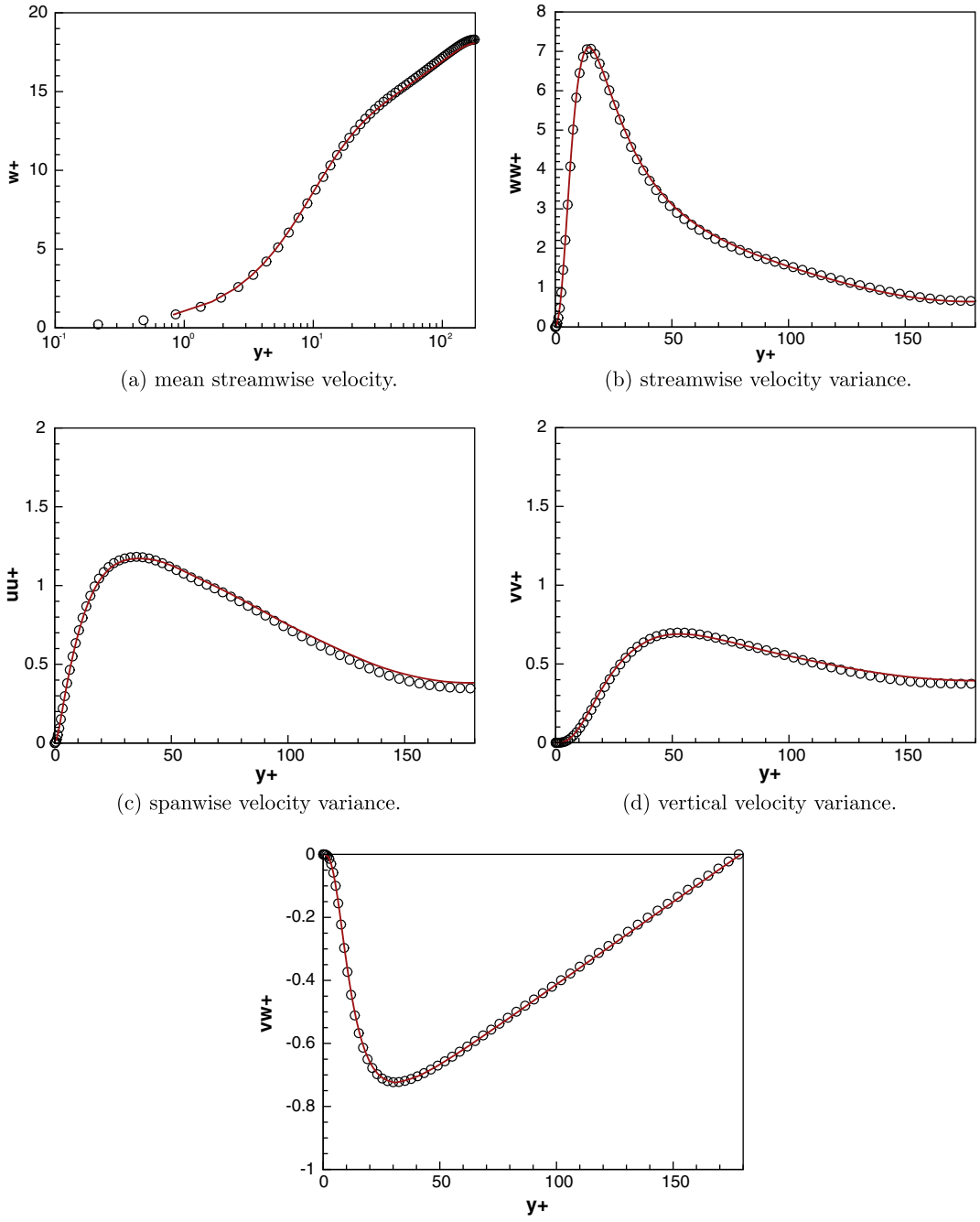

Fig. 6. Computed flow statistics for channel flow at $Re_\tau = 180$. The solid line and the symbol denote the present computation and the computation by Moser et al. [44], respectively.

5.1. DNS of fully developed turbulent flow in a channel

DNS of turbulent flow in a plane channel presents an excellent case for testing the spatial and temporal resolution of the method in a simple computational domain that can be handled in a straightforward manner using a body-fitted Cartesian grid.

DNS was carried out for turbulent channel flow at $Re_\tau = 180$. $Re_\tau = u_\tau h/\nu$ is Reynolds number based on the mean wall shear velocity and the channel half height (h), and ν is the viscosity. The size of the computational domain non-dimensionalized by the channel half height is 6.4, 3.2, and 2 in streamwise (z), spanwise (x), and vertical (y) directions, respectively, and a grid with $193 \times 129 \times 161$ is used to discretize the computational domain along these directions. The grid spacing in the spanwise and streamwise directions are 4.5 and 6 wall units, respectively. The minimum and maximum grid spacing in the vertical direction is 0.8 and 4.3 wall units, respectively. Periodic boundary conditions are employed in the streamwise and spanwise directions and the flow is driven by the constant pressure gradient imposed in the streamwise direction. The time step non-dimensionalized by the mean wall shear velocity and the viscosity is $\Delta t^+ = u_\tau^2 \Delta t/\nu = 0.07$, which corresponds to the CFL number of 0.1. A parabolic streamwise velocity profile with superimposed random fluctuations is prescribed as the initial condition. The simulation was first

Please cite this article in press as: Kang S et al. High-resolution numerical simulation of turbulence in natural waterways. Adv Water Resour (2010), doi:10.1016/j.advwatres.2010.09.018

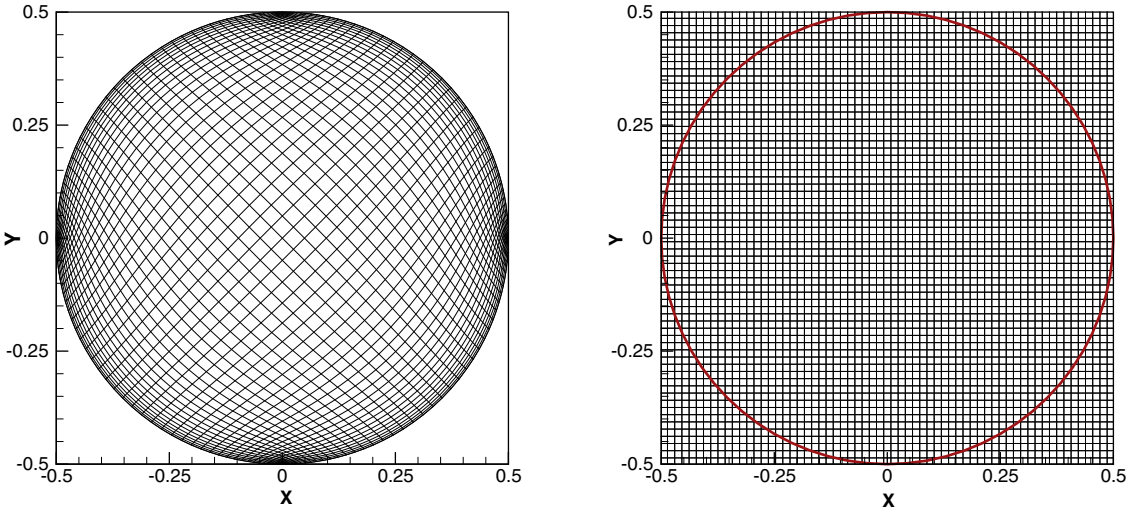

(a) 201×201 grid (every four grid lines are shown).

(b) 71 ×71 grid (the solid red line denotes the immersed boundary).

Fig. 7. Grids for the turbulent pipe flow computation.

run until the total kinetic energy of the computational domain reached steady-state. Following this, the simulation was continued and the solution was averaged for $t = 20$, which corresponds to about 48 flow through times. The computed mean flow and turbulence statistics are compared with those of the spectral DNS by Moser et al. [44] (Fig. 6). Even though the accuracy of the spatial discretization method of the present model is second-order, the agreement between the results of our computation and the spectrally accurate results of Moser et al. [44] is excellent.

5.2. RANS simulation of fully developed turbulent pipe flow

We simulate fully developed turbulent flow in a straight circular pipe using RANS models for turbulence closure. The objective of this test case is to demonstrate the accuracy of the boundary condition reconstruction approach in the CURVIB method described in Section 4. For that, we carry out simulations using both a curvilinear, near-wall resolving, boundary-fitted grid and the CURVIB approach with a wall model to apply boundary conditions on the pipe wall and compare the results of the two simulations. For both simulations, we employ the SST RANS model. The Reynolds number of the flow based on the bulk velocity and the diameter of the pipe is $Re = 4 \times 10^4$. The Navier–Stokes and turbulence closure equations are solved in a time accurate manner until the solution becomes steady state with periodic boundary condition specified in the streamwise direction.

The wall resolving RANS computation is carried out using the boundary-fitted, curvilinear grid shown in Fig. 7a to discretize the pipe cross-section. 201×201 grid points are employed and the near-wall grid spacing is about 1 wall unit. The no-slip boundary condition for the velocity and the low Reynolds number boundary conditions for k and ω are prescribed at the wall of the pipe.

The second simulation is carried out by immersing the wall of the pipe, discretized with a triangular mesh, in a uniform Cartesian grid with 71×71 grid points as shown in Fig. 7b. The pipe is treated as an immersed boundary and boundary conditions are specified using CURVIB method. The near-wall grid spacing for this case is about 40 wall units and is much coarser than the wall-resolving case. Therefore, velocity and turbulence quantities boundary conditions are reconstructed using the wall model described in Section 4.1.

In both simulations, four grid points are used in the streamwise direction and a constant streamwise pressure gradient is specified.

The computed non-dimensional streamwise mean velocity profiles for the two cases are shown in Fig. 8a and b and compared with the experimental results [45]. In the figure, r^+ implies the distance from the wall in wall units and W^+ is the mean streamwise velocity normalized by the mean shear velocity. For both cases excellent agreement is observed between calculations and measurements. As one would expect, the wall-resolving simulation captures the logarithmic, buffer and laminar sublayer regions of the velocity profile while the CURVIB wall-model simulation can only capture the outer part of the logarithmic region. The agreement between the computation and measurements is very good and demonstrates the correct implementation of the CURVIB wall-model in RANS mode.

5.3. LES and URANS of turbulent flow in a natural stream

To demonstrate the ability of the method to carry out high resolution simulations of flow in a natural stream with arbitrarily complex bathymetry, we apply it to carry out LES and URANS simulations of turbulent flow in the meandering stream currently installed in the St. Anthony Falls Laboratory Outdoor StreamLab (OSL), University of Minnesota, Minneapolis, MN, USA. This research facility (Fig. 9) is a 40-m by 20-m basin which has been configured into a sand-bed meandering stream channel that was approximately 50-m long, 2-m wide, and 0.1-m deep at base flow. Native riparian seedings were planted along the streambank during the first year of operation (2008) along with biodegradable coconut-fiber bank stabilization matting. By 2009, the vegetation had established stable root systems that, along with the remains of the initial coconut fiber matting, stabilized the bank position. The floodplain was seeded with a mixture of native prairie grass seed. Entrance conditions for the OSL allow accurate control and measurement of water and sediment discharge rates, and the facility is outfitted with a sedimentation basin at its downstream end where sediment is collected and stockpiled for recirculation. Simulations and measurements reported herein were performed for a flow rate of 4.45×10^{-2} m^3/s, which yields Reynolds and Froude numbers, based on average values of depth (0.1 m), velocity

Please cite this article in press as: Kang S et al. High-resolution numerical simulation of turbulence in natural waterways. Adv Water Resour (2010), doi:10.1016/j.advwatres.2010.09.018

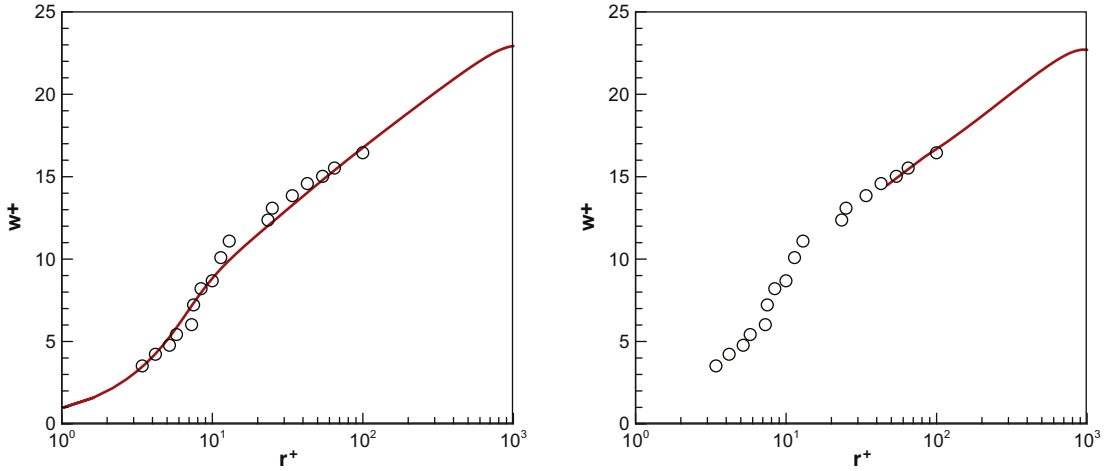

(a) 201 × 201 grid (wall resolving case). (b) 71 × 71 grid (wall modeling case).

Fig. 8. Comparison of the non-dimensional mean streamwise velocity (solid line: computation, symbol: Laufer [45]).

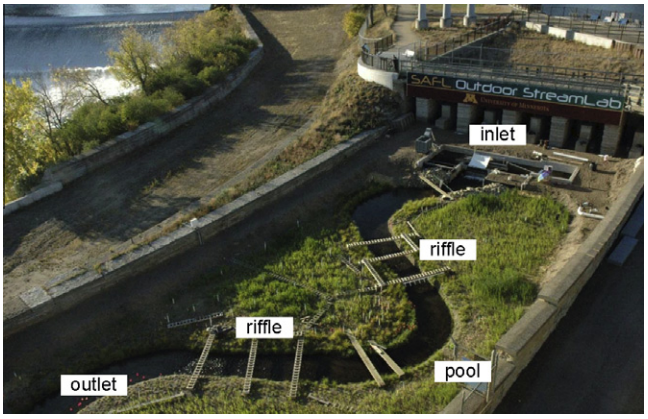

Fig. 9. Outdoor StreamLab.

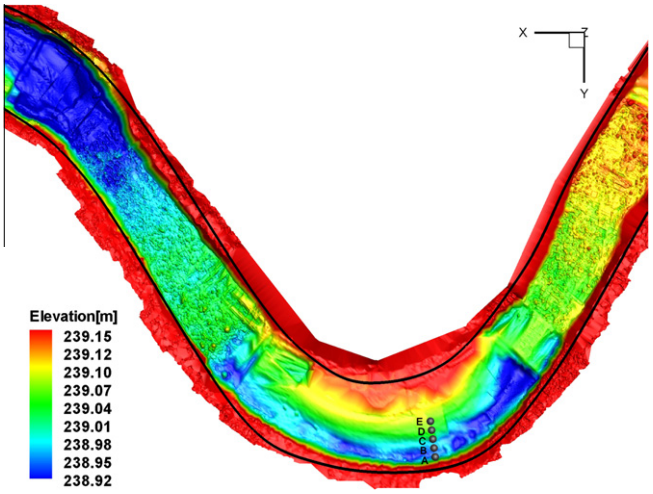

Fig. 10. The immersed body and the boundary of the background mesh for the OSL (the solid lines denote the boundary of the background mesh). The circles denote ADV measurement locations.

(0.23 m/s) and viscosity of the water (10^{-6} m^2/s), approximately equal to 2.3×10^4 and 0.23, respectively.

Three-dimensional mean velocity and turbulence statistics measurements in the OSL were obtained using acoustic Doppler Velocimetry (ADV; Nortek Vectrino and Sontek MicroADV) at 50 Hz for 5 min at each location. The ADV probes were mounted to a channel-spanning portable traverse enabling lateral and vertical positioning. At each cross-section, the position of this traverse was recorded using a total station (Sokkia X30RK), enabling registration of each sampling location within a common coordinate system. ADV measurements were obtained at 12 channel cross-sections located throughout the length of the stream: one directly upstream of the first riffle section, one across the midpoint of each riffle section, eight evenly spaced throughout the middle meander bend, and one spanning the apex of the downstream meander bend. At each cross section, vertical profiles were sampled every 0.25-m laterally at 0.05-m vertical spacing between sampling positions.

Bed and water surface topography in the OSL were collected on a 1-cm horizontal grid at sub-millimeter vertical accuracy using instruments mounted to a separate channel-spanning portable carriage, the position of which was registered using the total station. A laser distance sensor (Keyence LK-G series) was used for collecting subaerial bank topography, while a pulser and ultrasonic submersible transducer system (JSR Ultrasonics) documented subaqueous

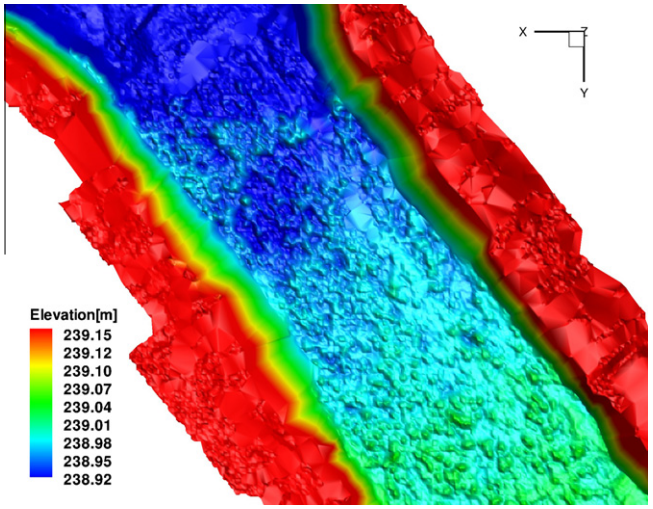

Fig. 11. The immersed body showing the bed roughness.

Please cite this article in press as: Kang S et al. High-resolution numerical simulation of turbulence in natural waterways. Adv Water Resour (2010), doi:10.1016/j.advwatres.2010.09.018

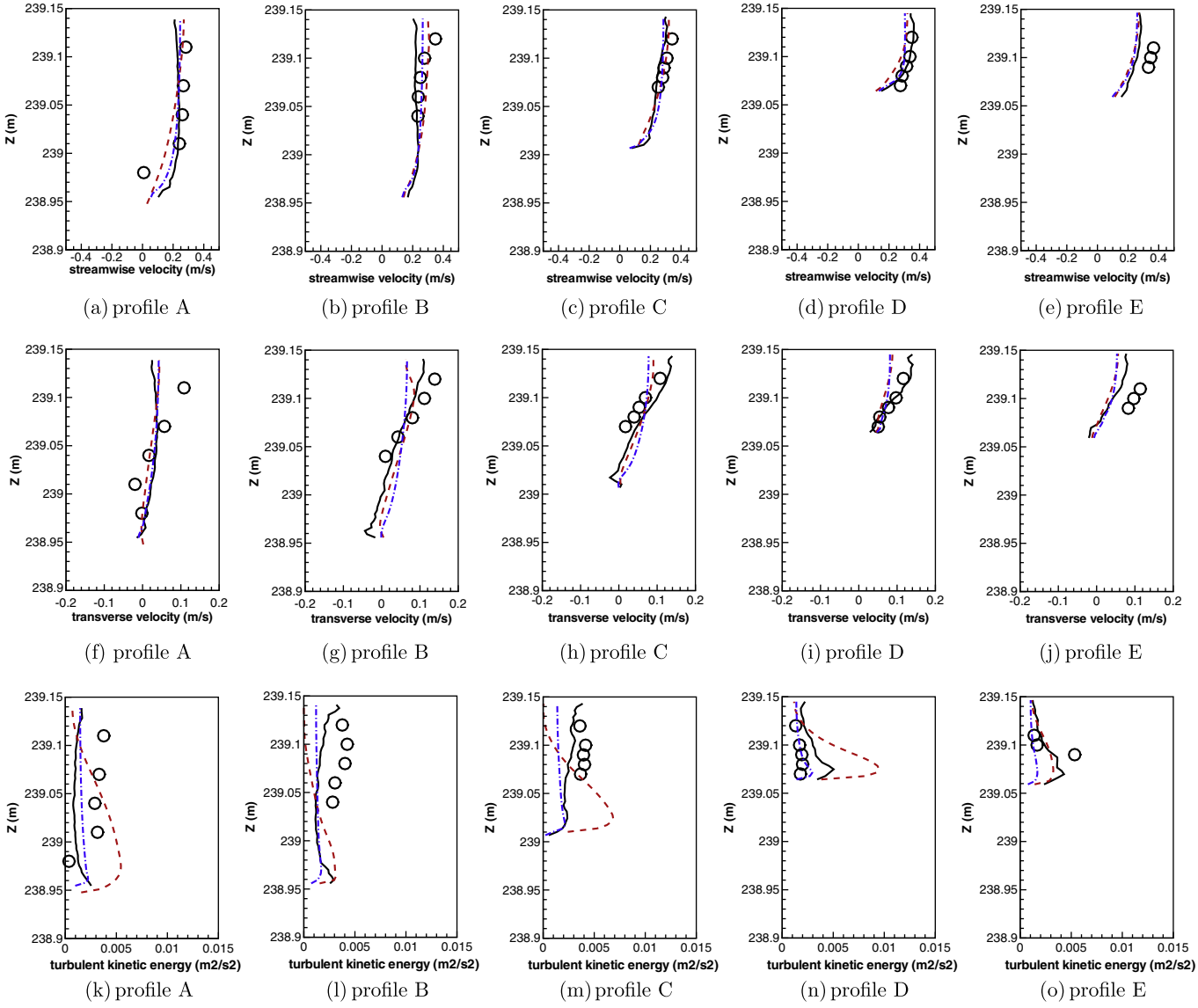

Fig. 12. Comparison of the mean streamwise velocity (the first row), the mean transverse velocity (the second row), and the turbulence kinetic energy (the third row) with the measurement (black solid line: LES, red dashed line: k–ω, blue dash dotted line: SST, symbol: measurement).

topography. Mean water surface elevation measurements were sampled at 50 Hz over a centimeter-scale spaced grid using an ultrasonic distance sensor (Massa).

The high-resolution scanned bathymetry of the OSL is shown in Fig. 10. The flow direction is from the right to the left and key features of the stream bathymetry include the two riffle zones, which occupy the straight parts between successive curved sections, and one pool zone in between. The measured bathymetry in one of the riffles is shown in Fig. 11 to illustrate the level of resolution of the various bed features. It is evident from this figure that the measurements resolve individual, centimeter-scale roughness elements on the bed. The measured bathymetry is discretized with an unstructured triangular mesh and embedded in an approximate meandering channel of rectangular cross-section as required by the CURVIB method. The outline of the background curvilinear domain is marked with the two black lines in Fig. 10.

The free surface is treated as a sloping rigid lid on which slip boundary conditions are imposed. This assumption is justified by the relatively low Froude number of the experimental flow. The shape of the free-surface boundary is prescribed from measurements of the mean water surface elevation.

The background curvilinear mesh discretizing the approximate meandering channel consists of 67 million grid nodes, with $3650 \times 301 \times 61$ nodes in the streamwise, lateral, and vertical directions, respectively. The grid spacing in the three directions is about 10 mm, 9 mm and 1 mm or approximately 100, 90 and 10 wall units in streamwise, transverse and vertical directions, respectively. The same grid is employed both for LES and URANS simulations. The wall modeling is used to compute the velocity boundary conditions at the IB nodes since the present simulation does not resolve the viscous sublayer. It is important to emphasize that the present wall model does not incorporate any roughness effects. This is because in the present geometry roughness elements are almost exclusively found in the two riffles where the computational grid we employ is sufficiently fine to directly resolve most of the key geometric features of the bed. As such, we treat the complex bed bathymetry as smooth wall and the presence of roughness is incorporated by resolving directly flow structures around individual, small scale obstacles, e.g. small rocks, on the stream bed.

For the LES at the inlet of the flow domain we feed instantaneous velocity fields obtained from a separate LES of fully developed flow in a straight open channel with the same cross-section

Please cite this article in press as: Kang S et al. High-resolution numerical simulation of turbulence in natural waterways. Adv Water Resour (2010), doi:10.1016/j.advwatres.2010.09.018

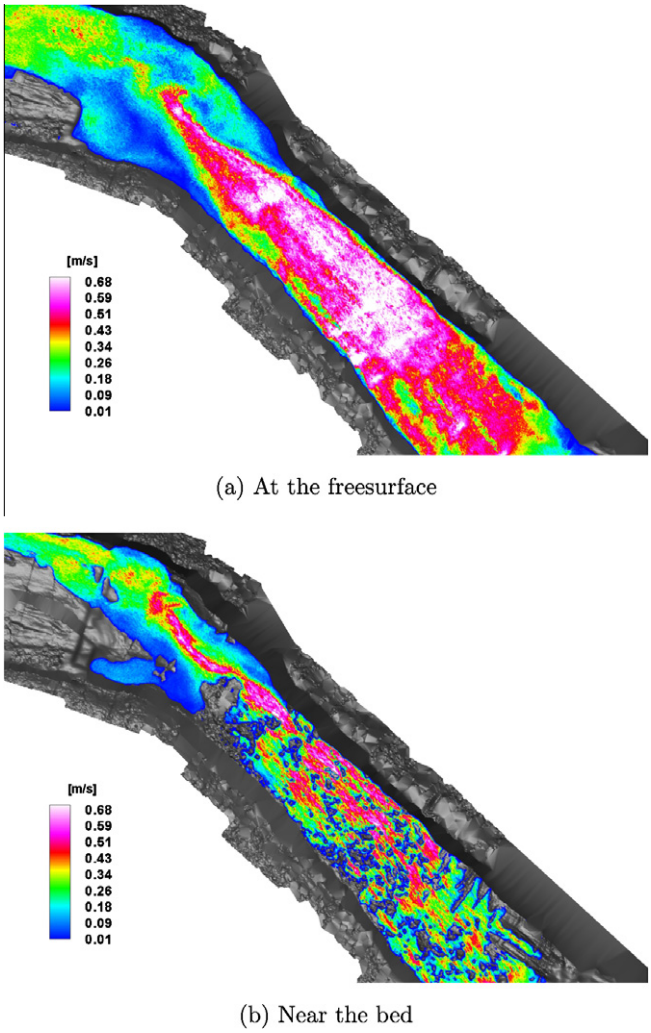

(a) At the freesurface

(b) Near the bed

Fig. 13. Instantaneous velocity magnitude computed by the LES model (flow direction: from the right to the left).

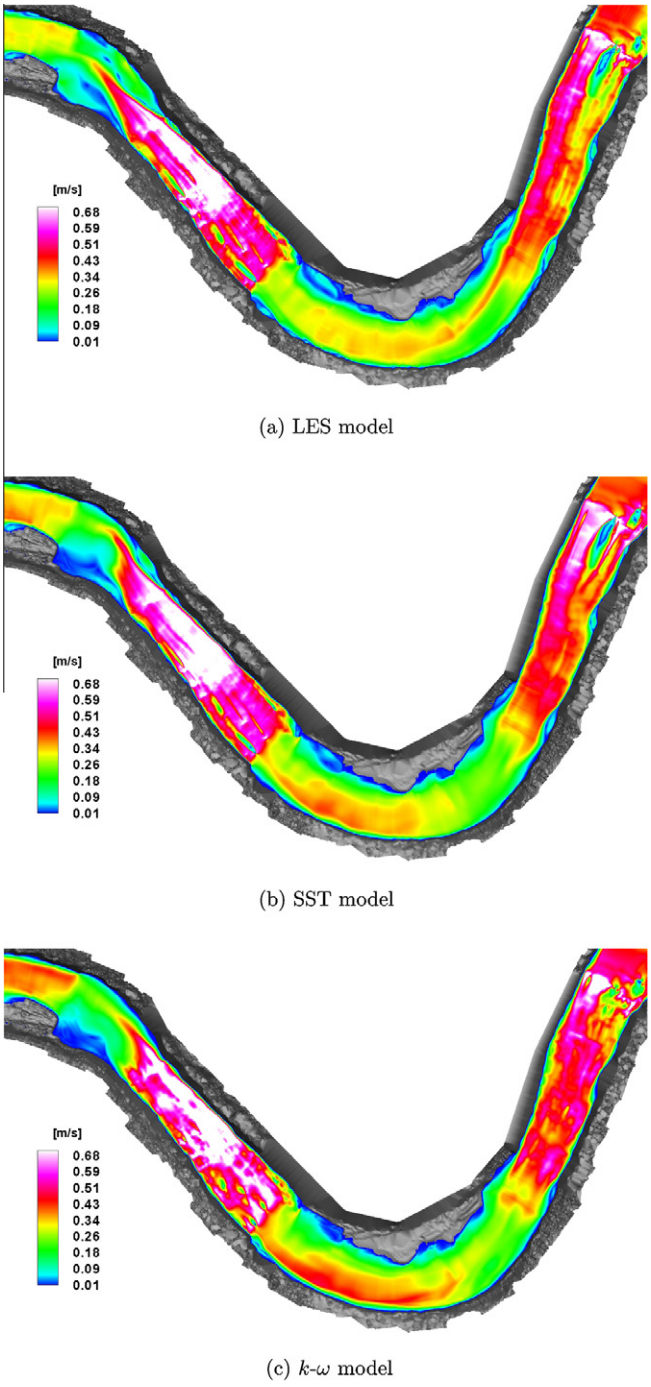

(a) LES model

(b) SST model

(c) k-ω model

Fig. 14. Computed mean velocity magnitude at the free surface.

as that of the inlet OSL cross-section at the same Reynolds number. For the URANS simulations, which are carried out using both the k–ω and SST models, we prescribed a plug flow mean velocity profile corresponding to the measured flow rate. For all simulations, the time step is chosen as 0.001 s which is equivalent to the CFL number of 0.5. The simulations were performed on a Linux cluster composed of 512 AMD Opteron 2.53 GHz processors and 160 processors were used for the simulations. The LES and RANS simulations were first run until the total kinetic energy in the computational domain reached steady-state and subsequently the flowfields were averaged for approximately $t = 40$ s and 5 s, respectively. The wall-clock time for the LES of $t = 40$ s (or 40,000 time steps) was about 10 days.

Fig. 10 shows few selected locations within the pool region where measured velocity and TKE profiles are compared with the computed results in Fig. 12. All models capture the mean streamwise (Fig. 12a–e) and transverse (Fig. 12f–j) velocity profiles with reasonable accuracy. This level of agreement is overall consistent with the reasonable agreement between the mean velocity contours at the water surface predicted by all three models in the region between the two riffles as shown in Fig. 14. The counter-clockwise secondary flow (the positive transverse velocity is toward the outer bank) is observed both in the computed and measured transverse velocity profiles suggesting that all three models capture correctly the magnitude of the secondary motion at least in the region where measurements were carried out. The agreement between the computed and measured TKE profiles (Fig. 12k–o) is not as good as that for the mean velocities but the LES and URANS–SST results are in better overall agreement with the measurements than the k–ω model, which over-predicts significantly the TKE magnitude near the bed.

Overall the agreement between the LES and URANS–SST computed results with the measurements is reasonable. This finding is especially encouraging when one takes into account the inherent uncertainties in carrying out measurements in a field scale stream like the OSL and the fact that all simulations were carried out without any calibration against the measured data.

Please cite this article in press as: Kang S et al. High-resolution numerical simulation of turbulence in natural waterways. Adv Water Resour (2010), doi:10.1016/j.advwatres.2010.09.018

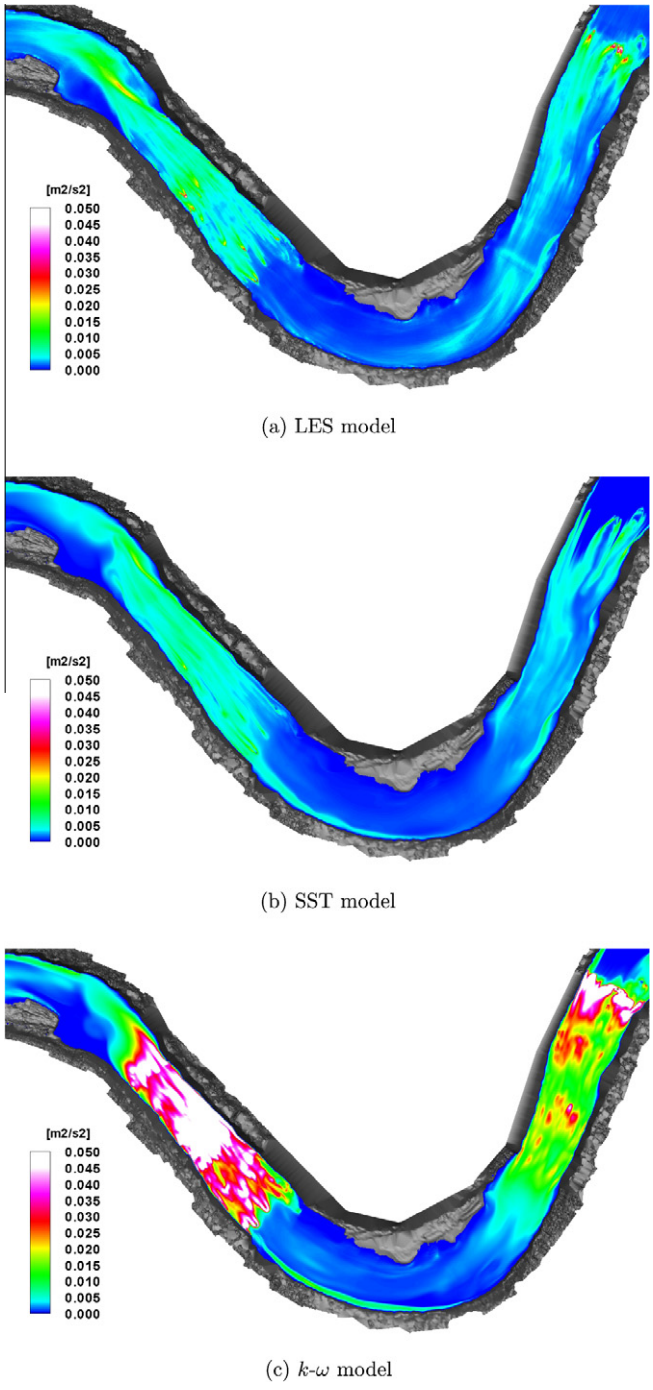

(a) LES model

(b) SST model

(c) k-ω model

Fig. 15. Computed turbulence kinetic energy at the free surface.

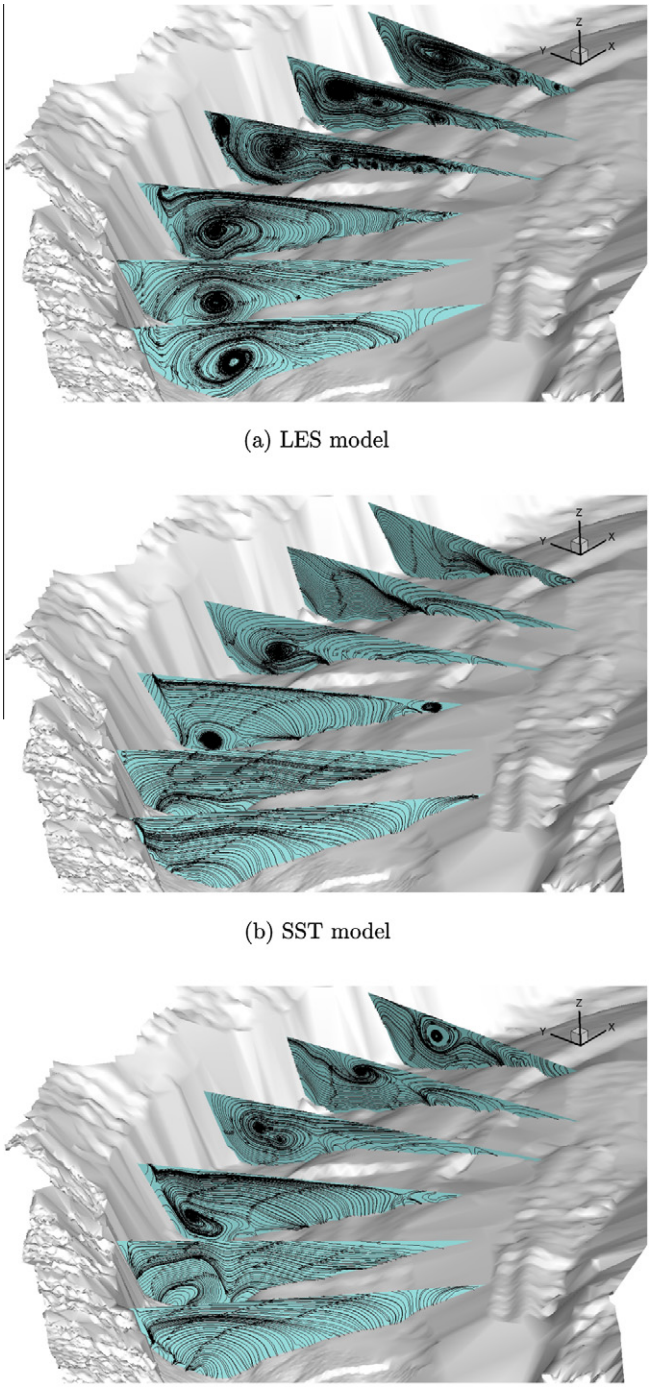

(a) LES model

(b) SST model

(c) k-ω model

Fig. 16. Computed 2D streamlines of the mean flow at cross-sections near the bend (looking downstream).

Snapshots of the calculated instantaneous flow fields at the free surface and near the bed in the riffle region obtained by the LES are shown in Fig. 13. It is evident from the figure that the LES resolves very complex flow features at the free-surface that are the result of the complex and highly heterogeneous bed bathymetry in the riffle region, including intense shear layers and regions of recirculation. The snapshot of the flow at the plane near the bed clearly demonstrates the ability of the method to simulate flow patterns around discrete roughness elements, such as high velocity streaks and vortex shedding around small-scale bed roughness.

Contours of mean velocity magnitude at the water surface computed by the LES and URANS models are shown in Fig. 14. The velocity magnitudes in the riffle zones predicted by the LES and the SST models are very similar to each other, while the k–ω model predicts overall higher velocity magnitudes. Some important differences among the three models are also observed in the pool region between the two riffles. The LES predicts the existence of a thin shear layer emanating from the inner bank and ultimately diffusing along the outer bank just upstream of the second riffle. This shear layer is presumably formed due to the sudden expansion of the cross-sectional area between the riffle and pool regions and the strong curvature of the bend. This feature of the flow is not captured by either URANS model.

Please cite this article in press as: Kang S et al. High-resolution numerical simulation of turbulence in natural waterways. Adv Water Resour (2010), doi:10.1016/j.advwatres.2010.09.018

The turbulence kinetic energy (TKE) contours at the surface computed by the LES and the two URANS models are shown in Fig. 15. The LES and the SST models yield qualitatively similar results and overall similar levels of TKE. A strikingly different prediction is obtained, however, by the k–ω model with the overall TKE levels in the two riffle regions being nearly one order of magnitude higher than those obtained by the LES and the SST model. Considering that the maximum measured TKE in the riffle zones was in the range of 0.01–0.02 m^2/s^2, the k–ω model significantly overpredicts the magnitude of the turbulence kinetic energy while the values predicted by the LES and the SST model are qualitatively correct. Durbin [46] pointed out that two equation models predict an anomalously large growth of TKE in stagnation point flow. Since the spatial resolution of the present simulations in the riffle zones is high enough to resolve discrete roughness elements, there are many stagnation regions in the flow (e.g. around each roughness element) where the non-physical TKE is produced. Since the SST model employs a limiter for the production term (Eq. (17)), its predictions do not suffer from this anomaly.

Fig. 16 shows the computed mean flow streamlines at selected 2D cross-sections near the bend. The LES result clearly shows the formation of the counter-clockwise secondary cells along the thalweg of the channel bed. The streamlines of the RANS models also show the secondary cells but they do not clearly show the existence of the helical motion.

6. Conclusions

A versatile numerical model for carrying out coherent-structure resolving simulations (URANS or LES) of turbulent flows in real-life natural streams has been developed and validated. A major feature of the model is that it employs a sharp-interface immersed boundary modeling framework, the CURVIB method developed in our group, and can thus handle the arbitrarily complex bathymetry of natural streams resulting from roughness elements and/or embedded natural and man-made structures. Wall modeling was incorporated in the context of the CURVIB method to enable LES and URANS simulations on grids that are not sufficiently fine to resolve the laminar sublayer. An important feature of the method is its computational efficiency, which made high-resolution 3D unsteady simulations in long and shallow open channels discretized with stretched, high-aspect-ratio meshes feasible. The efficiency of the method is derived from the fractional step approach employed to solve the incompressible Navier–Stokes equations in conjunction with the algebraic multigrid strategy implemented to accelerate the convergence of the Poisson equation for the pressure.

High resolution measurements of the SAFL OSL streambed were collected and used to construct a computational grid that resolves centimeter-scale roughness elements on the bed. No attempt was made to calibrate the numerical model for roughness since the simulations were able to resolve directly vortex shedding from individual small-scale roughness elements in the two riffle zones. Even though both URANS and LES yielded overall similar results for the mean velocity field some important discrepancies were observed in the predicted TKE fields. Namely, the k–ω model yielded TKE levels at the water surface in the riffle zones nearly one order of magnitude higher than those measured and calculated with LES and the SST model. This striking finding is attributed to the inherent limitation of two-equation, isotropic eddy-viscosity models in flows with regions of flow stagnation – the so-called stagnation point anomaly. The SST model does not suffer from this anomaly since it incorporates a limiter in the TKE production term. In the pool region in between the two riffles the LES and URANS models yielded overall similar results but the LES did predict the existence of a sharp shear layer emanating from the inner bend and spreading toward the outer bend, which was not evident in the two URANS predictions. Comparisons with mean velocity and turbulence statistics measurements obtained in the pool region showed that all three models yielded similar results for the mean velocity profiles but the k–ω model over-predicted the TKE near the bed. Overall, however, and given the uncertainties involved in obtaining measurements in a field-scale facility such as the OSL and the fact that no calibration of any of the three turbulence models was attempted the computed results were in reasonable agreement with the measurements.

Further algorithmic advances of the present model are currently under way. We have recently extended the numerical model to incorporate sediment transport modeling capabilities to enable future geomorphodynamics simulations (see [47]). Finally, we have also developed a coupled, nonlinear modeling framework using a two-phase flow, level-set approach for simulating water surface deformation. This new algorithm, which will be reported in a future communication, will enable us to eliminate the rigid-lid simplification incorporated in the present model and also do away with the need for prescribing the shape of the air–water interface from experimental data.

The numerical method we have developed herein is a powerful tool both for obtaining fundamental insights into the structure of turbulence in natural waterways and for improving the designs of hydraulic structures, such as bridge foundations and stream-restoration structures. In our future work we will carry out simulations for different flow conditions and for various embedded in stream structures to further validate the numerical model using measurements to be collected in the OSL. We will also analyze the LES flowfields to understand a number of complex phenomena in natural waterways, such as, among others, the dynamics of large-scale coherent vortices, the complex, multi-cellular structure of secondary motion in meander bends, and the effects of roughness transition regions such as those observed at pool-riffle interfaces.

Acknowledgments

This work was supported by NSF Grants EAR-0120914 (as part of the National Center for Earth-Surface Dynamics) and EAR-0738726 and a Grant from Yonsei University, South Korea. Computational resources were provided by the University of Minnesota Supercomputing Institute.

References

[1] Ge L, Sotiropoulos F. A numerical method for solving the 3D unsteady incompressible Navier–Stokes equations in curvilinear domains with complex immersed boundaries. J Comput Phys 2007;225(2):1782–809.
[2] Devenport WJ, Simpson RL. Time-dependent and time-averaged turbulence structure near the nose of a wing-body junction. J Fluid Mech 1990;210:23–55.
[3] Paik J, Sotiropoulos F. Coherent structure dynamics upstream of a long rectangular block at the side of a large aspect ratio channel. Phys Fluids 2005;17(11):115104.
[4] Sinha SK, Sotiropoulos F, Odgaard AJ. Three-dimensional numerical model for flow through natural rivers. J Hydraul Eng 1998;124(1):13–24.
[5] Wilson CAME, Boxall JB, Guymer I, Olsen NRB. Validation of a three-dimensional numerical code in the simulation of pseudo-natural meandering flows. J Hydraul Eng 2003;129(10):758–68.
[6] Rodriguez JF, Bombardelli FA, Garcia MH, Frothingham KM, Rhoads BL, Abad JD. High-resolution numerical simulation of flow through a highly sinuous river reach. Water Resour Manage 2004;18(3):1573–650.
[7] Lai YG, Weber LJ, Patel VC. Nonhydrostatic three-dimensional model for hydraulic flow simulation. I: Formulation and verification. J Hydraul Eng 2003;129(3):196–205.
[8] Zeng J, Constantinescu G, Blanckaert K, Weber L. Flow and bathymetry in sharp open-channel bends: experiments and predictions. Water Resour Res 2008;44(9):W09401.
[9] Spalart PR. Trends in turbulence treatments. AIAA Paper 2000-2306; 2000.

[10] Menter FR, Kuntz M, Langtry R. Ten years of industrial experience with the SST turbulence model. Turbul Heat Mass Transfer 2003;4:625–32.
[11] Ge L, Sotiropoulos F. 3D unsteady RANS modeling of complex hydraulic engineering flows. I: Numerical model. J Hydraul Eng 2005;131(9):800–8.
[12] Ge L, Lee SO, Sotiropoulos F, Sturm T. 3D unsteady RANS modeling of complex hydraulic engineering flows. II: Model validation and flow physics. J Hydraul Eng 2005;131(9):809–20.
[13] Hodges BR, Street RL. On simulation of turbulent nonlinear free-surface flows. J Comput Phys 1999;151(2):425–57.
[14] Zedler EA, Street RL. Large-eddy simulation of sediment transport: Currents over ripples. J Hydraul Eng 2001;127(6):444–52.
[15] McCoy A, Constantinescu G, Weber LJ. Numerical investigation of flow hydrodynamics in a channel with a series of groynes. J Hydraul Eng 2008;134(2):157–72.
[16] Stoesser T, Ruether N, Olsen NRB. Calculation of primary and secondary flow and boundary shear stresses in a meandering channel. Adv Water Resour 2010;33(2):158–70.
[17] Paik J, Escauriaza C, Sotiropoulos F. On the bimodal dynamics of the turbulent horseshoe vortex system in a wing-body junction. Phys Fluids 2007;19(4):045107.
[18] Spalart PR, Jou WH, Strelets M, Allmaras SR. Comments on the feasibility of LES for wings, and on a hybrid RANS/LES approach. In: Liu C, Liu Z, editors. Advances in DNS/LES. Columbus, OH: Greyden; 1997.
[19] Sagaut P. Large eddy simulation for incompressible flows. Berlin: Springer; 1988.
[20] Smagorinsky JS. General circulation experiments with the primitive equations. Mon Weather Rev 1963;91:99–164.
[21] Germano M, Piomelli U, Moin P, Cabot WH. A dynamic subgrid-scale eddy viscosity model. Phys Fluids A 1991;3(7):1760–5.
[22] Armenio V, Piomelli U. A Lagrangian mixed subgrid-scale model in generalized coordinates. Flow Turbul Combust 2000;65(1):51–81.
[23] Wilcox DC. Reassessment of the scale-determining equation for advanced turbulence models. AIAA J 1988;26:1299–310.
[24] Jiang GS, Shu CW. Efficient implementation of weighted ENO schemes. J Comput Phys 1996;126(1):202–28.
[25] Cabot W, Moin P. Approximate wall boundary conditions in the large-eddy simulation of high reynolds number flow. Flow Turbul Combust 2000;63(1–4):269–91.
[26] Wang M, Moin P. Dynamic wall modeling for large-eddy simulation of complex turbulent flows. Phys Fluids 2002;14(7):2043–51.
[27] Gilmanov A, Sotiropoulos F. A hybrid Cartesian/immersed boundary method for simulating flows with 3D, geometrically complex, moving bodies. J Comput Phys 2005;207(2):457–92.
[28] Saad Y, Schultz MH. GMRES: a generalized minimal residual algorithm for solving nonsymmetric linear systems. SIAM J Sci Stat Comput 1986;7(3):856–69.
[29] Brown PN, Saad Y. Hybrid Krylov methods for nonlinear systems of equations. SIAM J Sci Stat Comput 1990;11(3):450–81.
[30] Eisenstat SC, Walker HF. Choosing the forcing terms in an inexact newton method. SIAM J Sci Stat Comput 1996;17(1):16–32.
[31] Knoll DA, Keyes DE. Jacobian-free Newton–Krylov methods: a survey of approaches and applications. J Comput Phys 2004;193(2):357–97.
[32] Dennis JE, Schnabel RB. Numerical methods for unconstrained optimization and nonlinear equations. Englewood Cliffs, NJ: Prentice-Hall; 1983.
[33] Rosenfeld M, Kwak D, Vinokur M. A fractional step solution method for the unsteady incompressible Navier–Stokes equations in generalized coordinate systems. J Comput Phys 1991;94(1):102–37.
[34] Briggs WL, Henson VE, McCormick SF. A multigrid tutorial. 2nd ed. Philadelphia, PA, USA: Society for Industrial and Applied Mathematics; 2000.
[35] Naik NH, Rosendale JV. The improved robustness of multigrid elliptic solvers based on multiple semicoarsened grids. SIAM J Numer Anal 1993;30(1):215–29.
[36] Larsson J, Lien F, Yee E. Conditional semicoarsening multigrid algorithm for the Poisson equation on anisotropic grids. J Comput Phys 2005;208(1):368–83.
[37] Ruge JW, Stüben K. Algebraic multigrid. In: McCormick SF, editor. Multigrid methods. Frontiers in applied mathematics, vol. 3. Philadelphia: SIAM; 1987.
[38] Henson VE, Yang UM. BoomerAMG: a parallel algebraic multigrid solver and preconditioner. Appl Numer Math 2002;41(1):155–77.
[39] Sterck HD, Yang UM, Heys JJ. Reducing complexity in parallel algebraic multigrid preconditioners. SIAM J Matrix Anal Appl 2006;27(4):1019–39.
[40] Borazjani I, Sotiropoulos F. Numerical investigation of the hydrodynamics of carangiform swimming in the transitional and inertial flow regimes. J Exp Biol 2008;211(10):1541–58.
[41] Borazjani I, Sotiropoulos F. On the role of form and kinematics on the hydrodynamics of self-propelled body/caudal fin swimming. J Exp Biol 2010;213(1):89–107.
[42] Borazjani I, Sotiropoulos F, Malkiel E, Katz J. On the role of copepod antenna in the production of hydrodynamic force during hopping. J Exp Biol 2010;213(17):3019–35.
[43] Wilcox DC. Turbulence modeling for CFD. La Cañada, CA: DCW Industries; 1993.
[44] Moser RD, Kim J, Mansour NN. Direct numerical simulation of turbulent channel flow up to $Re_\tau = 590$. Phys Fluids 1999;11(4):943–5.
[45] Laufer J. The structure of turbulence in fully developed pipe flow. Tech. Rep. 1174, NACA; 1954.
[46] Durbin PA. On the k-3 stagnation point anomaly. Int J Heat Fluid Flow 1996;17(1):89–90.
[47] Khosronejad A, Kang S, Borazjani I, Sotiropoulos F. Curvilinear immersed boundary method for simulating flow field and sediment transport phenomena. Adv Water Resour, submitted for publication.

Please cite this article in press as: Kang S et al. High-resolution numerical simulation of turbulence in natural waterways. Adv Water Resour (2010), doi:10.1016/j.advwatres.2010.09.018